fluids

MDPI

Article

Mechanism of the Influence of Design Parameters on the Power Characteristics of a Multi-Stage Cup-Shaped Paddle Agitator Based on CFD Simulation

Jingmu Bai [1], Jian Sun [1], Yunfei Li [2,3], Hailun Ren [1,4,*], Qingzhao Liu [4,*], Wenhui Shen [2,*], Lu Wang [2,5], Weihong Li [4], Bingxin Zhu [5], Zheng Wang [5] and Yang Liu [6]

1 School of Petrochemical Engineering, Jilin University of Chemical Technology, Jilin 130015, China; 18740095299@163.com (J.B.); sunjian6225@126.com (J.S.)
2 Befar Group Co., Ltd., Bingzhou 256600, China; liyunfei@befar.com (Y.L.); wanglu@befar.com (L.W.)
3 Shandong Befar Binhe New Material Co., Ltd., Binzhou 256600, China
4 School of Energy and Chemical Engineering, Tianjin Renai College, Tianjin 301604, China; weihli@tju.edu.cn
5 School of Chemical Engineering and Technology, Tianjin University, Tianjin 300072, China; wangzheng_1@tju.edu.cn (Z.W.)
6 Jilin General Aviation Vocational and Technical College, Jilin 132211, China; liuyang1261@126.com
* Correspondence: hlren@tju.edu.cn (H.R.); qingzhao_liu2021@tju.edu.cn (Q.L.); shenwh@befar.com (W.S.)

Abstract

Agitator reactors are widely used in chemical production processes, and their structural design has a significant impact on power consumption. Therefore, this study performs numerical simulations of multi-stage cup-shaped paddle agitators with different geometric parameters, and discusses in detail the effects of the paddle spacing (S/H), the ratio of the upper paddle length to the reactor radius (L_s/R), the ratio of the lower paddle length to the reactor radius (L_x/R), and the ratio of the upper to lower paddle lengths (L_s/L_x) on the reactor's power characteristics and internal flow field. Equations were derived to relate the power number (Np) to parameters such as Re, L_s/R, and L_x/R. The study found that, at the same Reynolds number, torque exhibits a slight upward trend as the paddle spacing increases; the best mixing effect is achieved when S/H is 0.333. Based on this pitch, when L_s/R, and L_x/R exceed 0.67, the mixing process fails to form a stable and complete radial circulation; when L_s/R and L_x/R are less than 0.53, the high-velocity zone in the flow field decreases, leading to the formation of dead zones. Therefore, selecting a multi-stage cup-shaped impeller with an L_s/R value of 0.53, an L_x/R value of 0.53, and L_s/L_x of 1 can achieve better mixing results with lower power consumption. These findings provide a reference for the energy-efficient optimization design of multi-stage cup-shaped impeller mixers in industrial applications.

Keywords: CFD; cup-shaped paddle; power number; torque

Check for updates

Academic Editor: Surya Pratap Vanka

Received: 16 June 2026
Revised: 21 July 2026
Accepted: 28 July 2026
Published: 30 July 2026

Copyright: © 2026 by the authors. Licensee MDPI, Basel, Switzerland. This article is an open access article distributed under the terms and conditions of the Creative Commons Attribution (CC BY) license.

1. Introduction

Agitated reactors are widely used in chemical production processes. Depending on the geometric configuration of the impeller, they can be applied to a variety of processes, including reaction, polymerization, de-gassing, grinding, and biological fermentation [1–5]. In large-scale chemical production, power consumption is one of the key economic indicators used to evaluate production costs, and the geometric structure of the impeller largely determines the power consumption of the mixing system. Therefore, the structural design of the impeller is generally considered a critical factor in the design of mixing systems [6–8].

Based on their geometric structures, commonly used impeller types primarily include inclined-disc, helical, straight-disc, and helical-ribbed designs. In previous studies, research on stirring power characteristics relied on experimental methods, which were limited by long experimental cycles and high financial costs [9–12]. With the continuous advancement of computational technology, Computational Fluid Dynamics (CFD) methods, owing to their high computational efficiency and lower costs, can to some extent supplement certain experimental studies and are therefore widely applied in the design and optimization of impeller configurations [13–15]. Based on this method, researchers have conducted extensive systematic analyses of stirred reactors featuring various impeller types.

Ameur et al. [16] conducted a systematic study using CFD numerical simulations to investigate the flow energy efficiency of four types of near-wall agitators (Maxblend, anchor, gate, and double-helix belt) when agitating shear-thinning fluids with yield stress. The results indicate that the Maxblend impeller generates the highest flow velocity at the same power input, demonstrating optimal energy efficiency and the lowest power consumption; the anchor-type and gate-type impellers exhibit lower efficiency due to dominant tangential flow and insufficient axial pumping capacity; while the double-helix belt impeller improves mixing in the upper part of the tank, it consumes the most power. Guo et al. [17] investigated the power characteristics of a novel cup-shaped paddle mixer. Using experimental and CFD numerical simulation methods, they studied the effects of factors such as paddle shape, installation angle, baffle configuration, rotational speed, and fluid properties on power consumption. The results indicate that the hollow structure of the cup-shaped paddle mixer significantly reduces fluid flow resistance. Its power consumption is lower than that of traditional 45° inclined paddle mixers and Rushton turbines under all operating conditions. Furthermore, power consumption is positively correlated with the paddle inlet area and installation angle. At high Reynolds numbers, the presence of baffles significantly increases turbulence intensity and power consumption. Shuchun Zhao [18] and colleagues focused on the energy consumption, flow characteristics, and energy-saving optimization design of a novel cup-shaped paddle stirred tank reactor in liquid–liquid systems. Using computational fluid dynamics (CFD), they systematically investigated the effects of five geometric parameters (four dimensionless arc length parameters and paddle angle) on the power number, flow rate number, and flow patterns. Performance data were obtained through CFD simulations and validated experimentally. The results indicate that the optimized cup-shaped paddles achieve 38% energy savings compared to conventional radial-flow impellers at the same flow rate, validating their high-efficiency energy-saving potential in liquid–liquid dispersion and reaction processes. Xiuhu Dang and colleagues [19] investigated the performance of cup-shaped paddle agitators in solid–liquid dissolution and gas–liquid mass transfer processes. The results indicate that in solid–liquid systems, the CB2-type impeller exhibits optimal dissolution performance under conditions of no baffles, low installation height, and a paddle angle of 22.5°. In gas–liquid systems, the axial flow configuration with a paddle angle of 15° demonstrates the highest mass transfer coefficient and gas saturation at the same power consumption. Compared with traditional 45° inclined-paddle impellers and Rushton turbines, the cup-shaped paddle mixer demonstrated superior mass transfer performance under the same energy consumption conditions. Furthermore, the study established dimensionless correlations for solid–liquid and gas–liquid mass transfer coefficients with high fitting accuracy, providing a theoretical basis for the industrial design and scale-up of this type of mixer. Pan Zhang [20] and colleagues investigated the performance of cup-shaped paddle agitators during the downward dispersion of lightweight particles. Using a combination of experiments and CFD-DPM numerical simulations, they systematically examined the effects of parameters such as paddle structure, diameter, deflection angle, clearance height,

solid content, particle size, and liquid viscosity on the critical dispersion speed and power consumption. The study demonstrated that, under optimal structural parameters (CB2-type paddles, diameter 0.43 m, deflection angle -30°, and clearance height of 1/4 of the liquid level), the cup-shaped paddle mixer can significantly reduce the critical dispersion speed and energy consumption, particularly exhibiting superior dispersion performance compared to traditional radial-flow RT and axial-flow PBT mixers in systems with high solid content (up to 40 *wt%*) and high-viscosity systems. Furthermore, when the solid content exceeds 10 *wt%*, interparticle collisions and gravitational compaction become the dominant dispersion mechanisms, causing the critical speed and power consumption to stabilize; powder-like particles are the most difficult to disperse due to agglomeration and poor wettability.

Compared to traditional single-stage mixing, multi-stage mixing breaks down a single mixing process into multiple synergistic functional stages by incorporating multiple layers of agitators or zone control within the same mixing equipment, ensuring uniform macroscopic flow throughout the tank; this approach ensures uniform macroscopic flow throughout the vessel while providing optimal shear force and turbulence intensity for different process stages (such as solid–liquid suspension, gas–liquid dispersion, and high-viscosity mixing), thereby avoiding the energy waste and material shear damage caused by "over-mixing" [21–25]. This approach extends equipment lifespan while reducing overall energy consumption and is suitable for fine chemical, biopharmaceutical, and new materials synthesis scenarios that demand high mixing quality and have narrow process windows. It serves as a key technological means for enhancing production efficiency and product quality.

Věříšová, M. et al. [26] conducted a systematic experimental study on the heat transfer performance of multistage agitators in jacketed mixing vessels. Using a multistage agitation system combining curved-paddle turbines with inclined-paddle impellers (three- or four-paddled), the researchers determined the heat transfer coefficients at different agitator spacings using transient methods. By combining numerical solutions and nonlinear regression in **MATLAB R2016a**, they established empirical heat transfer equations correlated with the Nusselt number, Reynolds number, Prandtl number, and viscosity ratio. The study found that the two-parameter regression model exhibited higher fitting accuracy at low Reynolds numbers, while the differences in heat transfer intensity and power consumption among the various agitator configurations were minimal, indicating similar energy efficiency. The results provide Nusselt number correlation parameters for six geometric configurations and suggest that, in the absence of relevant data, results from a single configuration can be used as an engineering approximation, offering an important reference for the design of biochemical reactors and food processing equipment. Alexander Heyter and Stefan Wollny [27] systematically investigated the influence of baffle geometric parameters on the power characteristics and mixing efficiency of multistage axial mixing systems. By varying the number, width, installation angle, and immersion depth of the baffles, and in combination with the dimensionless baffle characteristic number (BW), they quantitatively characterized the power numbers and mixing times of Rushton turbines and inclined-paddle propellers (PBTs) in both single-stage and multistage configurations. The results indicate that the commonly used four-baffle configuration (BS/D = 0.08) is insufficient to achieve a fully baffled state. Particularly for high-power-number mixers, baffle parameters must be adjusted according to the mixer type and diameter ratio. Inclined baffles ($\beta = 60^{\circ}$) reduce the baffle effect by approximately 22% compared to vertical baffles, necessitating the introduction of a corrected shape factor to accurately describe their drag characteristics. The study further reveals that significant interactions exist between multi-stage axial agitators, with their actual power number being far lower than the sum of the single-stage power

numbers; moreover, mixing time can be accurately predicted using the Liepe cycle time model in conjunction with the actual power number. The study systematically quantified the coupled effects of baffle geometric parameters on power input, proposed a corrected shape factor for inclined baffles, and extended the applicability of the Liepe model to most multistage mixing systems, providing a theoretical basis and engineering guidance for the design and scale-up of mixing equipment. Shaodong Qin et al. [28] addressed issues such as dead zones and mixing inhomogeneity in high-viscosity fluids within conventional mixing tanks, as well as low flux and susceptibility to clogging in microchannel reactors, by proposing a continuous microfluidic multistage mixer and systematically investigating its mixing performance. The study employed a parallel competitive iodate/iodide reaction system as a chemical probe and combined UV spectrophotometry with ANSYS Fluent-based numerical simulation to systematically analyze the effects of stirring speed, fluid viscosity, and the number of stirring stages on mixing efficiency. The results indicate that increasing the stirring speed significantly improves mixing uniformity; when the speed is increased from 30 rpm to 200 rpm, the mixing index increases by an average of 98%. Higher fluid viscosity significantly reduces mixing efficiency, particularly under low-speed conditions. Increasing the number of mixing stages helps improve mixing performance, but optimization must take into account both fluid viscosity and energy consumption.

In summary, research on the flow characteristics and power consumption of traditional single-paddle agitators has been sufficiently thorough, particularly regarding the design of cup-shaped paddles, for which the relevant process design parameters have also been well-established. While multistage agitation has a wide range of applications in industrial production, current research on multistage cup-shaped agitators is limited. The influence of relevant design parameters (S/H, L_s/R, L_x/R, and L_s/L_x) on power consumption and flow field characteristics remains unclear and requires urgent investigation. Therefore, this study performs three-dimensional modeling of multi-stage cup-type mixers with different design parameters and conducts numerical simulations of their power consumption and flow field characteristics based on CFD theory. It discusses in detail the effects of various design parameters on power consumption and flow field characteristics, and fits the correlation equations between Np and the values of L_s/R, L_x/R, $S/L_{(s,x)}$, and $C/L_{(s,x)}$ as a function of Re. The results obtained can provide a theoretical foundation for the industrial optimization design of multistage cup-type mixers.

2. Model Development

2.1. Theoretical Method

In previous studies, the core advantage of the RNG k-ε model stems from the additional term (R_ε) in its ε-equation and the model constants derived from renormalization group theory [29,30], which enable it to dynamically respond to changes in the flow strain rate. Particularly in rotating and swirl flows, this model effectively corrects the turbulent viscosity through the additional term, significantly mitigating the excessive diffusion problem commonly found in the standard k-ε model. Consequently, it can more accurately predict the turbulent structure and separation behavior in regions of strong swirl, high-curvature walls, and recirculation zones [31,32]. Therefore, the standard RNG k-ε model was selected in this study to simulate a multistage cup-shaped stirred reactor, as shown in the continuity Equation (1).

$$\frac{\partial ui}{\partial xi} = 0 \tag{1}$$

In which u_i represents the instantaneous velocity component, and i = 1, 2, 3 correspond to the x, y, and z directions, respectively. The momentum equation is shown in Equation (2).

$$\rho(\frac{\partial ui}{\partial t} + uj\frac{\partial ui}{\partial xj}) = -\frac{\partial p}{\partial xj} + \frac{\partial}{\partial xj}[(\mu + \mu t)(\frac{\partial ui}{\partial xj} + \frac{\partial uj}{\partial xi})] \quad (2)$$

In which ρ is the fluid density, μ is the kinematic viscosity, μ_t is the turbulent viscosity coefficient, and p is the pressure. The transport equations for the RNG k-ε turbulence model are shown in Equations (3) and (4).

$$\frac{\partial(\rho k)}{\partial t} + \frac{\partial xj}{\partial(\rho ujk)} = \frac{\partial}{\partial xj}[(\mu + \frac{\mu t}{\sigma k})\frac{\partial k}{\partial xj}] + Gk - \rho\varepsilon \quad (3)$$

In which $G_k = \mu tS^2$ is the turbulent kinetic energy term generated by the gradient of the mean velocity and is the magnitude of the mean strain rate tensor.

$$\frac{\partial(\rho\varepsilon)}{\partial t} + \frac{\partial(\rho uj\varepsilon)}{\partial xj} = \frac{\partial}{\partial xj}[(\mu + \frac{\mu t}{\sigma\varepsilon})\frac{\partial\varepsilon}{\partial xj}] + C1\varepsilon\frac{\varepsilon}{k}Gk - C_{2\varepsilon}^{*}\rho\frac{\varepsilon^2}{k} \quad (4)$$

In which $C_{2\varepsilon}^{*}$ is a key correction term in the *RNG* model $C_{2\varepsilon}^{*} = C_{2\varepsilon} + \frac{C_\mu\,\eta^3(1-\eta/\eta_0)}{1+\beta\eta^3}$, $\eta = S\frac{k}{\varepsilon}$ is the ratio of strain rate to the turbulent time scale, $\eta_0 \approx 4.38$, and $\beta = 0.012$. Unlike the standard k-ε model, the RNG model solves for the eddy viscosity coefficient using differential equations; however, the algebraic formula commonly used in standard implementations is $\mu_t = \rho C_\mu \frac{k^2}{\varepsilon}$, where the model constant is $C_\mu = 0.0845$. The standard constants for the RNG k-ε model are as follows (derived from RNG theory): $C_{1\varepsilon} = 1.42$, $C_{2\varepsilon} = 1.68$, $\sigma_k = 0.7194$, and $\sigma_\varepsilon = 0.7194$.

2.2. Geometry of Stirred Reactors

The geometric configuration of the multi-stage cup-shaped stirred reactor is shown in Figure 1. The reactor is 0.36 m high and 0.3 m in diameter, with both L_s and L_x equal to 0.1 m; the impellers are spaced 120° apart. The tip of each paddle is designed in a cup shape and rotates counterclockwise; structural details are shown in Figure 2. Other detailed design parameters for the different impellers are shown in Tables 1 and 2.

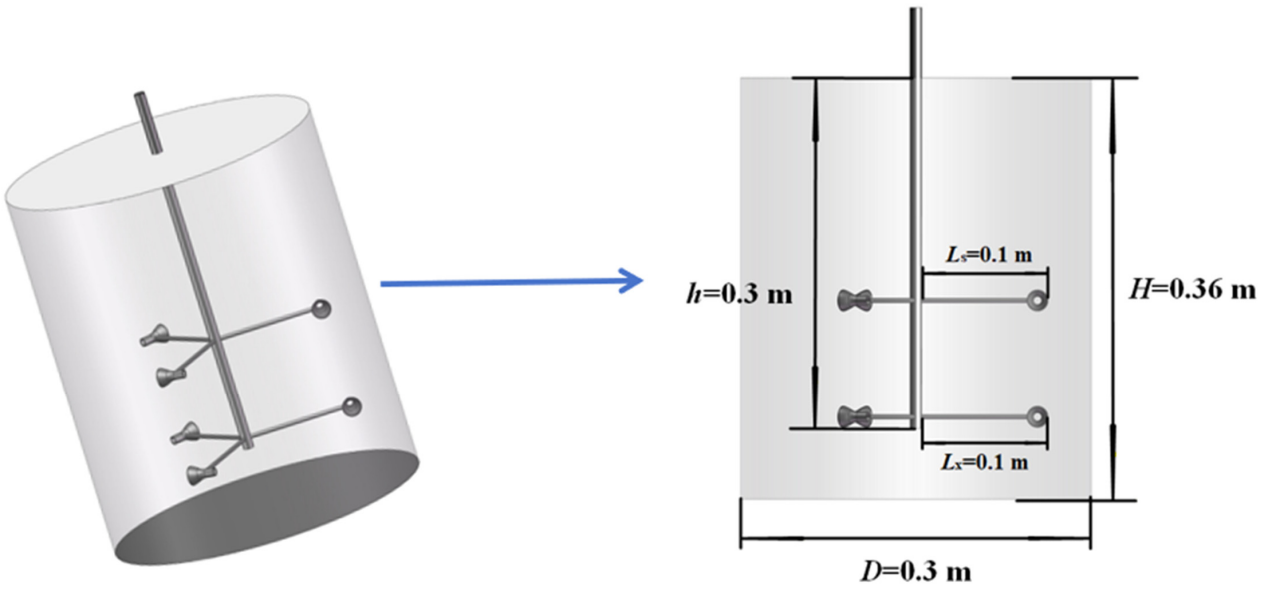


Figure 1. Geometric model of a multistage stirred reactor.

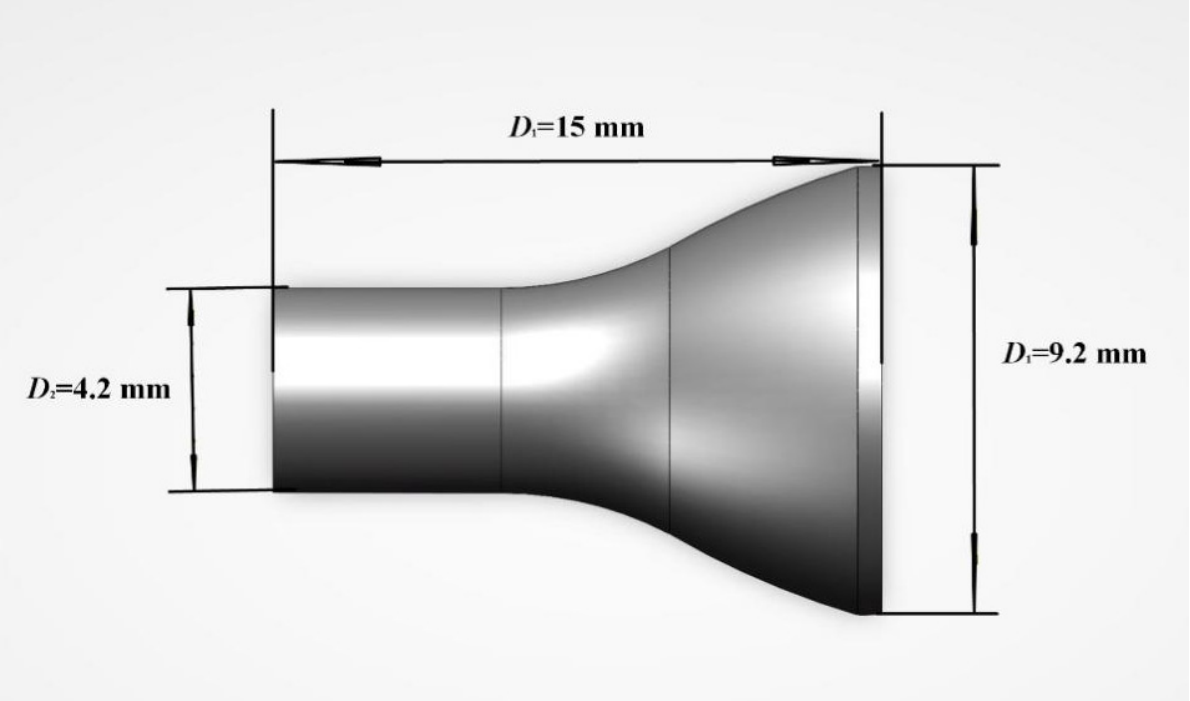


Figure 2. Geometric model of a cup-shaped structure.

Table 1. Different Pitch Models.

Paddle Type	Geometry	L_s/L_x (mm)	S (mm)	H (mm)	S/H	C (mm)
BX-JJ-50		100	50	300	0.166	60
BX-JJ-75		100	75	300	0.25	60
BX-JJ-100		100	100	300	0.333	60
BX-JJ-125		100	125	300	0.416	60

Table 1. *Cont.*

Paddle Type	Geometry	L_s/L_x (mm)	S (mm)	H (mm)	S/H	C (mm)
BX-JJ-150		100	150	300	0.5	60
BX-JJ-175		100	175	300	0.583	60

Table 2. Models with Different Paddle Lengths.

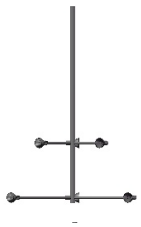
Paddle Type	Geometry	R (mm)	L_x (mm)	L_s (mm)	L_x/R	L_s/R
BX-100-s40x120		150	120	40	0.8	0.267
BX-100-s60x120		150	120	60	0.8	0.4
BX-100-s80x120		150	120	80	0.8	0.533
BX-100-s100x120		150	120	100	0.8	0.667

Table 2. *Cont.*

Paddle Type	Geometry	R (mm)	L_x (mm)	L_s (mm)	L_x/R	L_s/R
BX-100-s120x120		150	120	120	0.8	0.8
BX-100-s40x100		150	100	40	0.667	0.267
BX-100-s60x100		150	100	60	0.667	0.4
BX-100-s80x100		150	100	80	0.667	0.533
BX-100-s100x100		150	100	100	0.667	0.667
BX-100-s120x100		150	100	120	0.667	0.8
BX-100-s40x80		150	80	40	0.533	0.267

Table 2. *Cont.*

Paddle Type	Geometry	R (mm)	L_x (mm)	L_s (mm)	L_x/R	L_s/R
BX-100-s60x80		150	80	60	0.533	0.4
BX-100-s80x80		150	80	80	0.533	0.533
BX-100-s100x80		150	80	100	0.533	0.667
BX-100-s120x80		150	80	120	0.533	0.8
BX-100-s40x60		150	60	40	0.4	0.267
BX-100-s60x60		150	60	60	0.4	0.4
BX-100-s80x60		150	60	80	0.4	0.533

Table 2. *Cont.*

Paddle Type	Geometry	R (mm)	L_x (mm)	L_s (mm)	L_x/R	L_s/R
BX-100-s100x60		150	60	100	0.4	0.667
BX-100-s120x60		150	60	120	0.4	0.8
BX-100-s40x40		150	40	40	0.267	0.267
BX-100-s60x40		150	40	60	0.267	0.4
BX-100-s80x40		150	40	80	0.267	0.533
BX-100-s100x40		150	40	100	0.267	0.667
BX-100-s120x40		150	40	120	0.267	0.8

2.3. Simulation Details and Mesh Independence Verification

As shown in Figure 3a, the fluid domain within the reactor is divided into two parts: a rotating domain and a stationary domain. Both sections consist of unstructured tetrahedral elements, which are well-suited for handling complex models. Therefore, this type of mesh

was used for the meshing approach. A Multi-Reference-Frame (MRF) steady-state method was used to simulate a multistage stirred reactor. The interface was set to "no slip," and stationary walls were used to simulate the relative motion of the fluid flow. The rotational speed of the inner rotating region was set within the range of 100–1100 rpm. The top surface of the model was defined as a pressure outlet, the side and bottom surfaces as walls, and the gravitational acceleration along the Z-axis was set to $-9.8\ m/s^2$. The simulated fluid was water (density 998.2 kg/m^3, viscosity 0.001003 Pa·s). ANSYS Mesh was used for mesh generation, with an average element quality of 0.83 or higher. A pressure-based solver was selected, using the default SIMPLE algorithm and a second-order upwind scheme to solve the equations. To ensure the accuracy of the results, the convergence tolerance was set to 10^{-5}, and all other parameters used the default values in ANSYS Fluent.

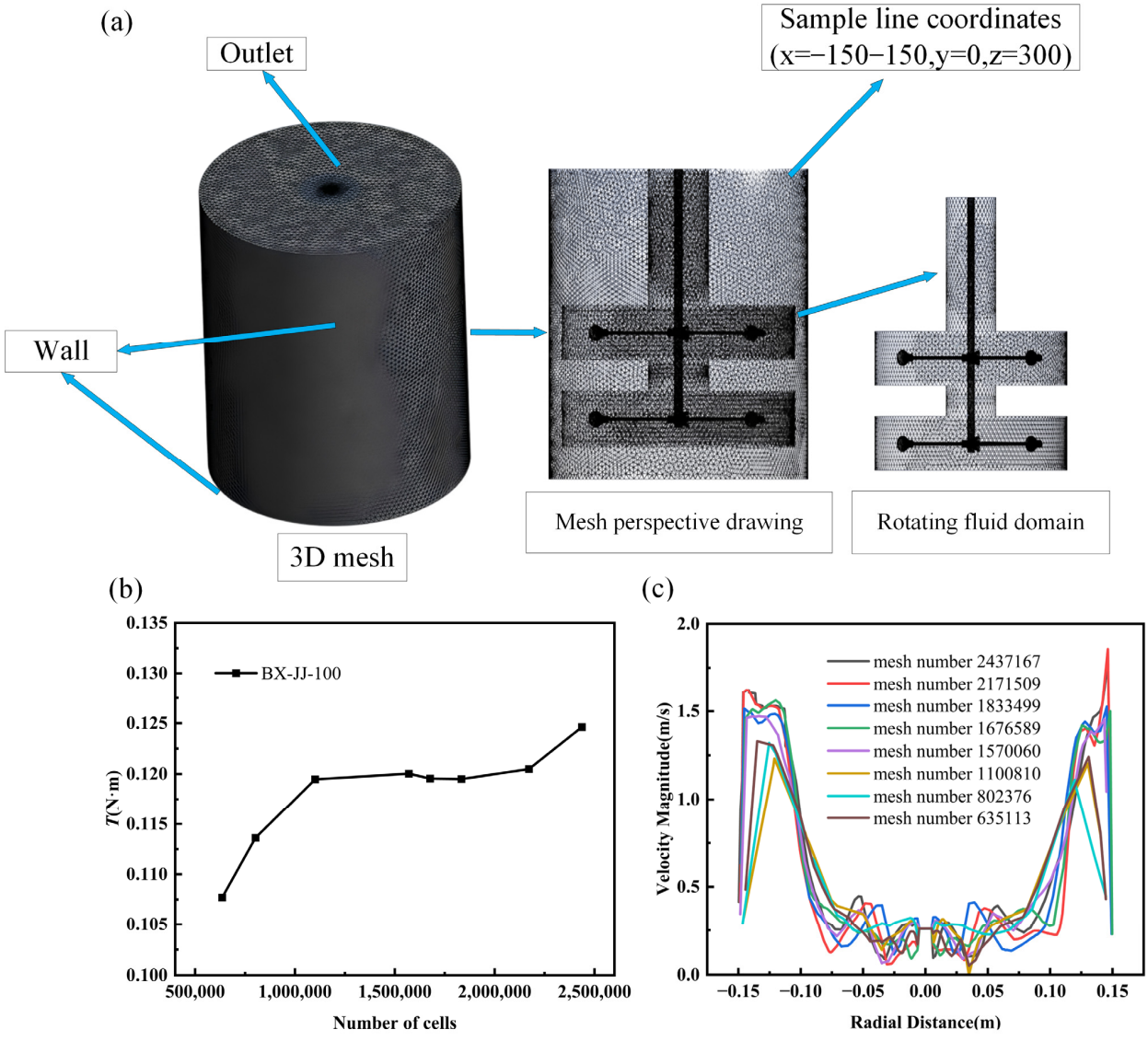


Figure 3. Mesh model and mesh independence validation diagram. (**a**) Schematic diagram of the mesh model (**b**) Effect of the number of mesh elements on torque (**c**) Effect of the number of mesh elements on speed.

Since the modeling of the cup-type stirrer exhibits geometric similarity, a cup-type stirrer model with a paddle spacing of 100 mm and upper and lower paddle lengths of 100 mm was selected for the grid-independence verification; the grid settings for the remaining models were consistent with those of this model. The total torque and velocity distribution

of the mixing system were selected as the primary criteria for the grid independence test, with the sampling line for the velocity distribution having a z-coordinate of +300 mm, a y-coordinate of 0, and an x-coordinate range of −150 to 150 mm. The torque results are shown in Figure 3b, with the number of similar mesh elements being 1,676,589, 1,833,499, and 2,171,509. Compared to the mesh with 2,437,167 elements, the torque errors for these three meshes were 4.7%, 4.2%, and 3.4%, respectively. The velocity distribution along the sample line is shown in Figure 3c. Among the velocity distribution curves for different samples, the meshes with 1,676,589, 1,833,499, and 2,171,509 exhibit a better fit. Considering both result accuracy and computation time, the grid model with 2,171,509 elements was ultimately selected for the final calculation; the remaining models have similar structures, so the mesh partitioning can remain consistent.

2.4. Model Validation

The numerical simulation methods used in this paper (turbulence models, discretization schemes, solution algorithms, etc.) fully follow the well-established simulation framework developed by Liu et al. [33,34], which has been validated using their experimental data. To confirm the accuracy of the simulation setup in this paper, we reproduced the standard validation conditions described in their paper for verification. Figure 4 shows a comparison of the experimental torque and the simulated torque. The average error between the simulation results and the experimental data was less than 20% [35,36], indicating good agreement and demonstrating that this numerical method can be applied to the operating conditions studied in this paper. Although the structure of the agitator blade in the validation experiments differs from that of the simulated agitator blade in this study, it still serves to demonstrate the reliability of the simulation model; such a validation approach has been widely accepted [37,38].

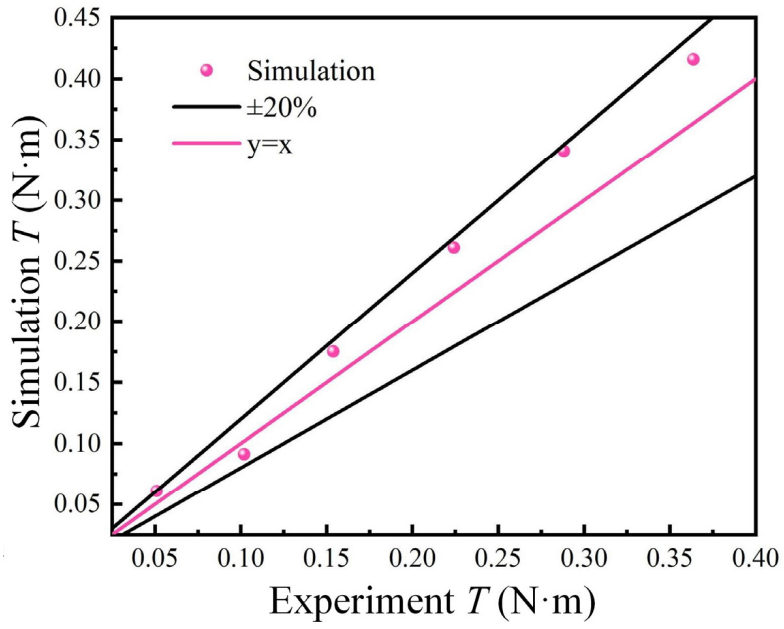


Figure 4. Comparison Chart of Experimental Torque and Simulated Torque.

3. Results and Discussions

3.1. Analysis of Power and Flow Fields for Paddles with Different S/H Ratios

Figure 5a shows the torque of impellers with different S/H ratios as a function of Reynolds number. As the Reynolds number increases, the torque of the impeller gradually increases. This is because the increase in rotational speed leads to an increase in the

tangential force in the rotational direction; to overcome this tangential force and reach the target rotational speed, a greater torque is inevitably required. At the same Reynolds number, the torque of paddles with different S/H ratios exhibits a slight upward trend, indicating that the paddle pitch has a negligible effect on torque.

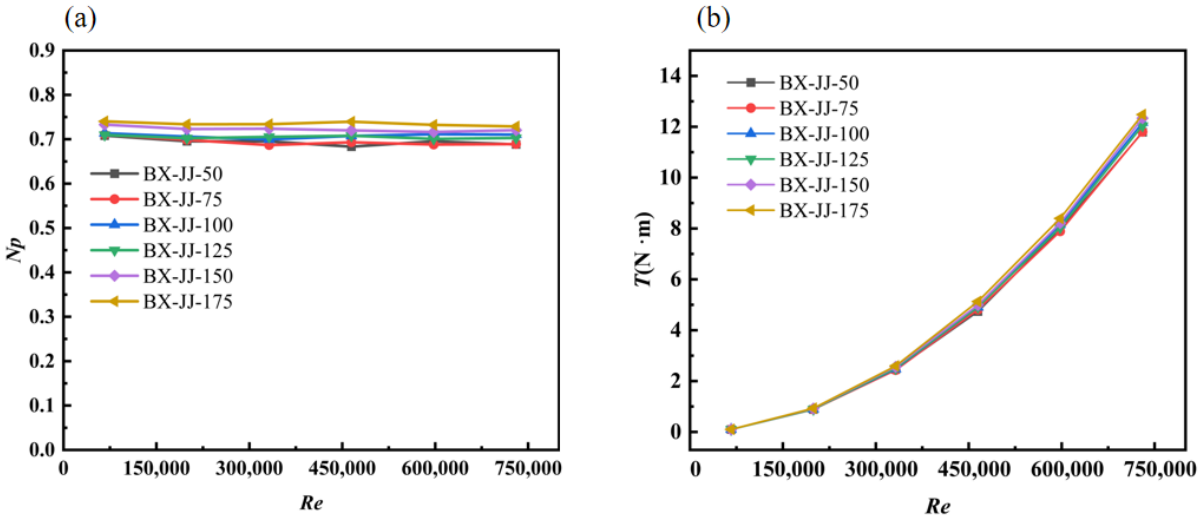


Figure 5. (**a**) Variation in paddle torque with Reynolds number for different S/H ratios. (**b**) Variation in paddle power coefficient with Reynolds number for different S/H ratios.

The power number is an important parameter used to characterize the power characteristics of a paddle. Figure 5b shows the variation in the paddle power number with Reynolds number for different S/H ratios. The figure shows that, at the same Reynolds number, the power number increases as the S/H ratio increases. As the Reynolds number increases, the power number gradually stabilizes and remains nearly constant, consistent with the trends reported by Guo, Steiros, and others [17,39]. This indicates that as the Reynolds number increases, its influence on the power number diminishes.

Figure 6 shows the velocity vector diagrams for different impeller spacings. It can be seen that changes in impeller spacing have no significant effect on the maximum rotational speed at the impeller tips. When S/H is less than 0.333, although the discharge flow from the upper propeller can provide a "boost" to the lower propeller, reducing the energy consumption associated with repeated fluid acceleration and resulting in lower overall power consumption, the turbulent wake vortices generated by the upper and lower impellers come close to each other. This creates a large area of high-speed turbulent mixing between the two impellers, preventing the formation of effective vortices between the two propellers. When S/H is greater than 0.333, as the impeller spacing increases, the wake vortices of the two impellers separate from each other. This not only allows each impeller to form its own independent circulation zone and overcome the tangential forces, leading to an increase in torque and power, but also causes the high-speed regions between the impellers to gradually separate. Consequently, circulation vortices form at the top of the mixing tank for different impeller spacings. Furthermore, as S increases, the top circulation vortex gradually shrinks, and the vortices between the impellers also become less pronounced as S increases, making it difficult to form a complete circulation. Both of these factors lead to poorer mixing efficiency. When S/H equals 0.333, four stable vortices form near both sides of the twin impellers, and the two wake vortices between the impellers have minimal mutual influence. This trend is consistent with the findings of Gao et al. [35].

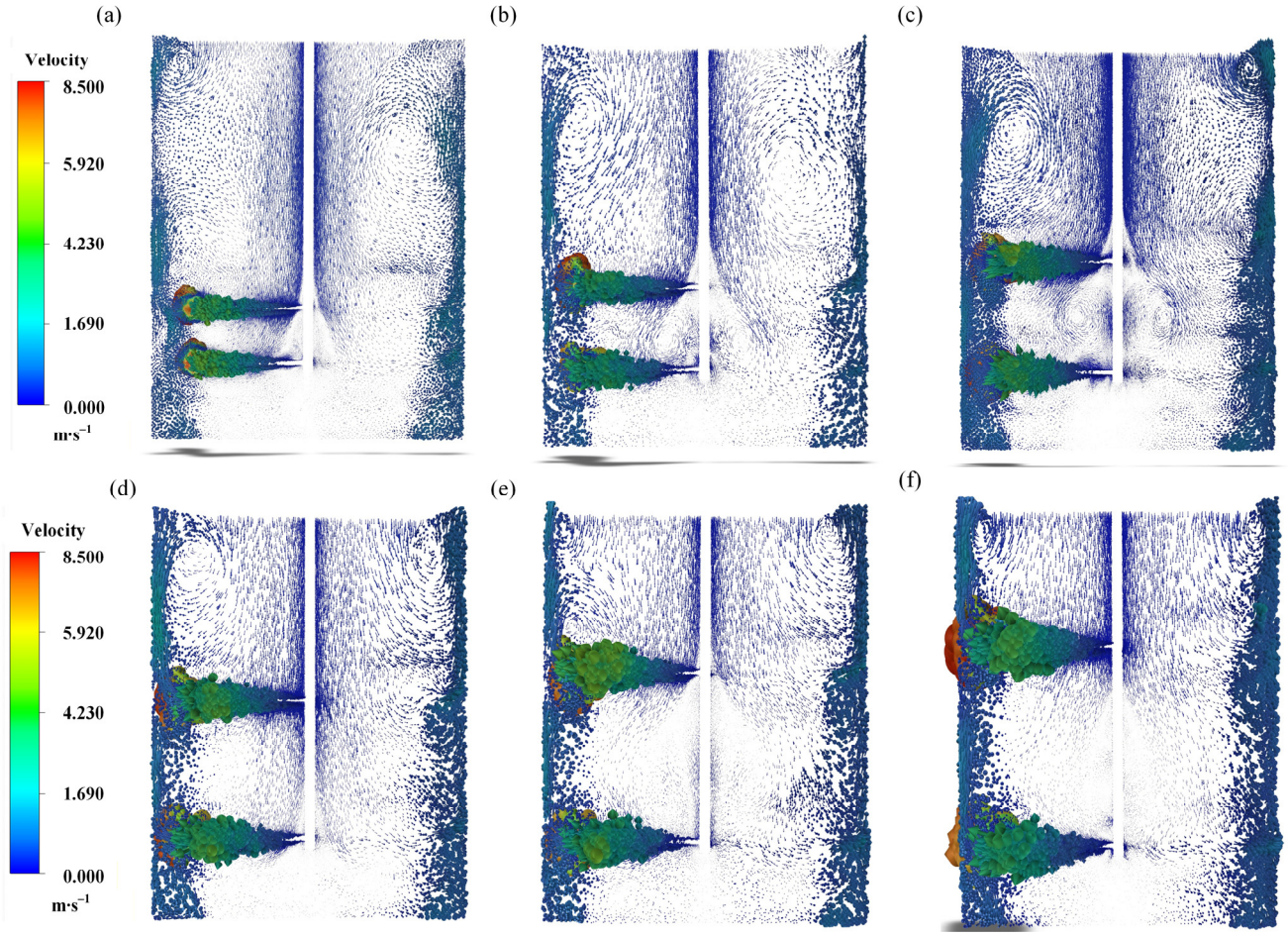


Figure 6. Velocity vector plots for different impeller spacings: (**a**) S = 50, (**b**) S S = 75, (**c**) S = 100, (**d**) S = 125, (**e**) S = 150, (**f**) S = 175.

Figure 7 shows the distribution of the internal turbulence dissipation rate in the reactor for different impeller configurations. Areas of high turbulence dissipation are concentrated in the core of the impeller jet, indicating intense fluid shear and excellent microscopic mixing efficiency in this region. Near the reactor bottom wall and at the corners of the liquid surface, the dissipation rate is below 0.01 m^2/s^3, forming mixing dead zones. A comparison of the various operating conditions shows that when S/H is less than 0.333, although there is no dead zone between the two impellers, the dead zone between the impeller shafts and the reactor top encompasses almost the entire upper space near the stirring shafts, leading to reduced mixing efficiency. When S/H is greater than 0.333, as the impeller spacing increases, although the dead zone at the top is gradually reduced, the dead zone between the twin impellers gradually expands. When S/H equals 0.333, the dead zone between the impellers is small, and the top dead zone is also partially reduced, resulting in the smallest total dead zone area.

After comparing various S/H values, we found that the mixing effect was optimal at an S/H ratio of 0.333, with moderate torque; therefore, we selected this spacing as the modeling standard for subsequent experiments.

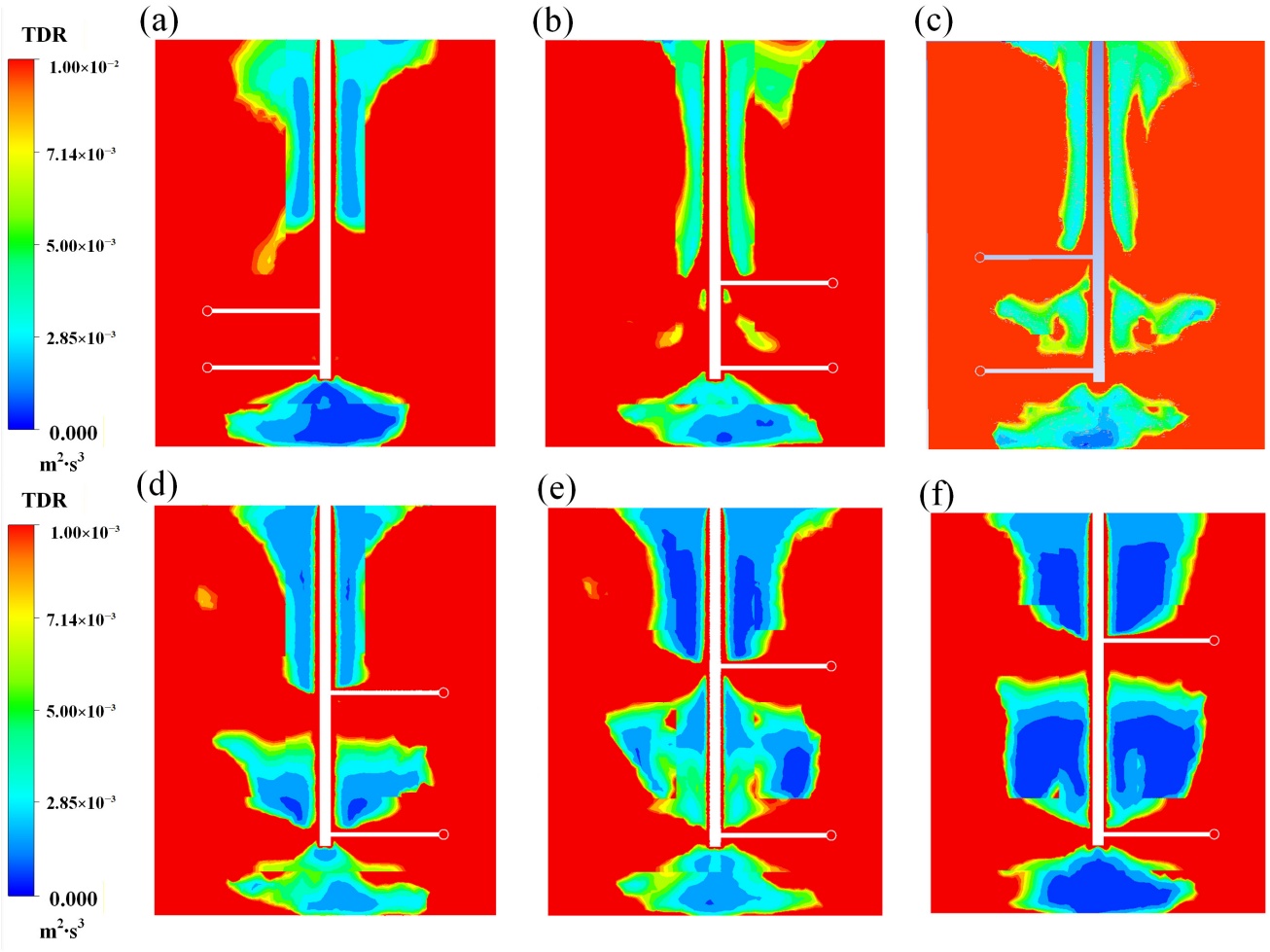


Figure 7. Distribution map of turbulence dissipation rates at different impeller spacings: (**a**) S = 50, (**b**) S = 75, (**c**) S = 100, (**d**) S = 125, (**e**) S = 150, (**f**) S = 175.

3.2. Power Analysis of Paddles with Different L_s/R and L_x/R Ratios

Figures 8 and 9 show the variation in paddle torque with Reynolds number for paddles with different L_s/R and L_x/R ratios. At different Reynolds numbers, the torque of paddles with different L_s/R and L_x/R ratios increases as the Reynolds number increases. At a given Reynolds number and a fixed L_x/R ratio, the paddle torque increases as the L_s/R ratio increases. Similarly, when the L_s/R value is fixed, the paddle torque also increases with an increase in the L_x/R value. When both L_s/R and L_x/R values increase or decrease, the paddle torque increases or decreases accordingly. This indicates that in a multistage mixing system, the total torque is determined jointly by the L_s/R and L_x/R ratios of the upper and lower stages. This is due to power superposition in multistage mixing systems; an increase in the diameter of any single stage of paddles leads to an increase in the torque required by that stage, which is directly added to the total torque, causing it to rise.

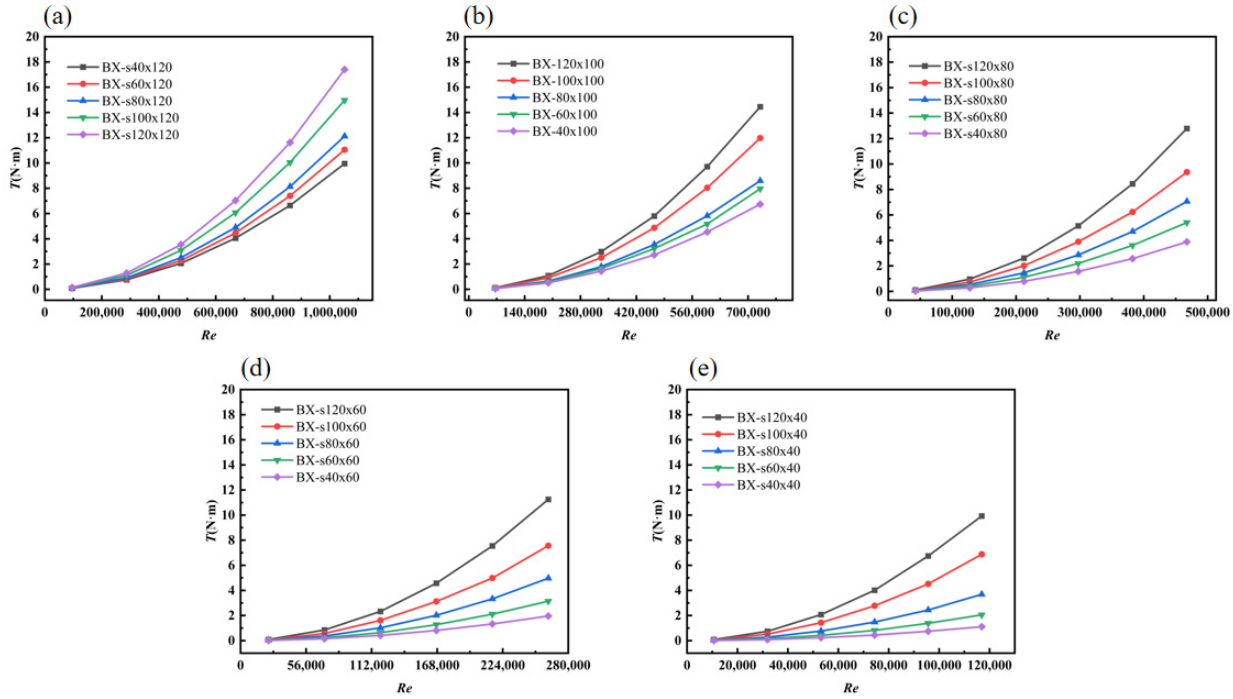


Figure 8. Variation in paddle torque with Reynolds number for different L_s/R values. (**a**) L_x = 120 (**b**) L_x = 100 (**c**) L_x = 80 (**d**) L_x = 60 (**e**) L_x = 40.

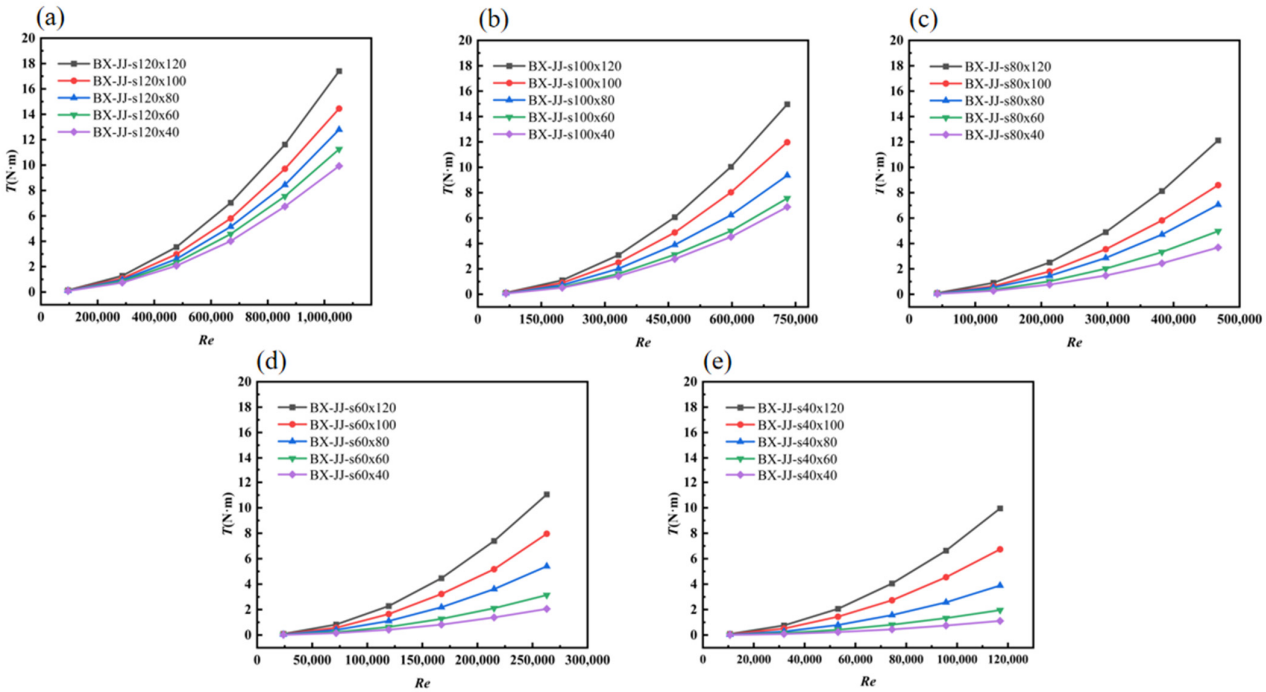


Figure 9. Variation in paddle torque with Reynolds number for different L_x/R values. (**a**) L_s = 120 (**b**) L_s = 100 (**c**) L_s = 80 (**d**) L_s = 60 (**e**) L_s = 40.

Figure 10 shows the power of paddles with different L_s/R and L_x/R values as a function of Reynolds number. As the Reynolds number increases, the power gradually approaches a constant value. At the same Reynolds number, the higher the ratio of L_s/R to L_x/R (L_s/L_x)—and the closer it is to 1—the higher the power output, reaching a maximum when it equals 1. This implies that energy consumption also increases. When the ratio of L_s/L_x is greater than 1, power decreases as this ratio increases; when the ratio is less than

1, power decreases as this ratio decreases. The reason for this is that when the lengths of the upper and lower paddles differ, the longer paddle determines the lower limit of the stirring power. As the ratio of L_s/L_x increases, the lower paddle becomes progressively shorter, and its impact on the overall power gradually decreases. Similarly, as the ratio of L_s/L_x decreases, the upper paddle becomes progressively shorter, and its influence on the overall power decreases until it approaches infinitely short lengths, at which point the overall power can be regarded as that of a single-paddle impeller. When the ratio of L_s/L_x approaches 1, since the upper and lower paddles are of equal length, fluid resistance increases, requiring more total power to drive the entire system, resulting in a higher overall power value.

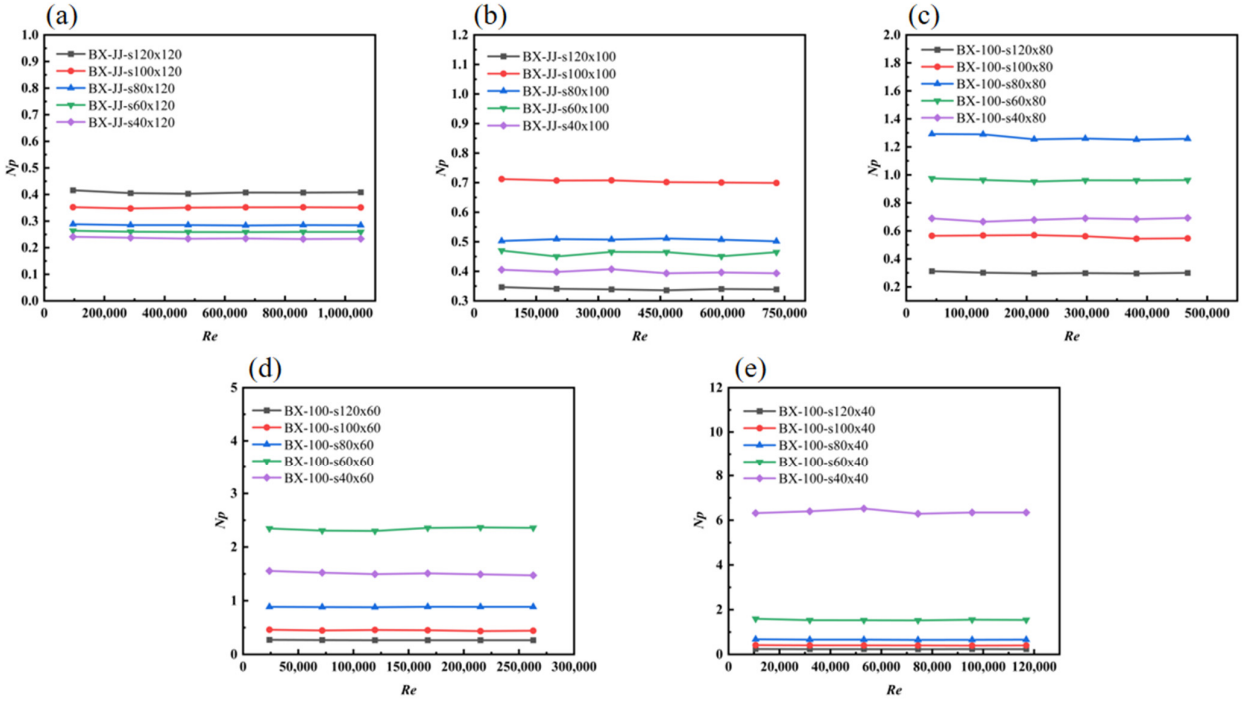


Figure 10. Variation in paddle torque with Reynolds number for different L_s/R and L_x/R values. (**a**) L_x = 120 (**b**) L_x = 100 (**c**) L_x = 80 (**d**) L_x = 60 (**e**) L_x = 40.

This paper derives the *Np*-*Re* relationship for multi-stage cup-type mixers with impellers of different lengths, in terms of the parameters L_s/R, L_x/R, $S/L_{(s,x)}$, and $C/L_{(s,x)}$. In a multistage impeller system, the *Np* number is generally calculated using the radius of the longest impeller in the system; therefore, the auxiliary dimensionless parameters S/L and C/L are used to precisely define the relative positions of the impellers in the multistage mixing system. The corresponding equations are as follows, and the correlations are shown in Figure 11.

$Np = 0.00341Re^{-0.01221}(L_s/R)^{0.55736}(L_x/R)^{-0.04256}(S/L_x)^{13.57049}(C/L_x)^{-10.85351}$, with an error within 18% (the formula applies to *Re*: 10,627–1,051,809, L_s/R: 0.267–0.667, L_x/R: 0.4–0.8, S/L_x: 0.83–1.25, C/L_x: 0.5–1, R^2 = 0.99637).

$Np = 7.70332\ Re^{-0.01135}(L_s/R)^{7.35203}(L_x/R)^{0.57915}(S/L_s)^{11.78473}(C/L_s)^{-1.61086}$, with an error within 18% (the formula applies to *Re*: 10,627–1,051,809, L_s/R: 0.4–0.8, L_x/R: 0.267–0.667, S/L_s: 0.83–1.67, C/L_s: 0.5–1, R^2 = 0.98868).

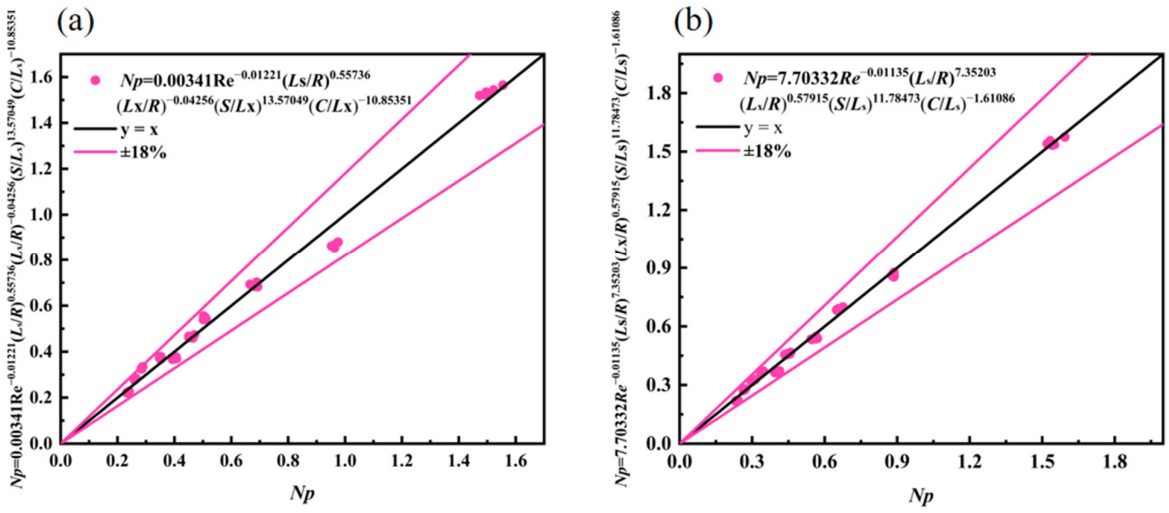


Figure 11. (**a**) *Np* correlations for paddles with different L_s/R and L_x/R ratios when $L_s/L_x \leq 1$. (**b**) *Np* correlations for paddles with different L_s/R and L_x/R ratios when $L_s/L_x \geq 1$.

3.3. Flow Field Analysis of Paddles with Different L_s/R and L_x/R Ratios

The velocity variations in the paddle for different L_s/R and L_x/R values are shown in Figure 12. In the single-layer flow field, the high-velocity region is primarily concentrated in the cup-shaped area. As the L_s/R and L_x/R values increase, the velocity field in the cup-shaped portion of the paddle also increases. Taking the upper laminar flow field as an example, when L_s/R is greater than 0.67, the flow velocity in the cup-shaped portion increases with increasing L_s/R values. However, because the cup-shaped region at the paddle tip in the upper flow field is very close to the reactor wall, the high-speed radial flow generated during mixing results in some velocity loss due to impact with the wall. Consequently, a stable and complete radial flow circulation cannot be formed, and the mixing efficiency is lower than theoretically expected. The same phenomenon is observed in the lower flow field when L_x/R exceeds 0.67. Conversely, as the L_s/R and L_x/R values decrease, the velocity field in the cup-shaped portion of the paddles also diminishes. When L_s/R is less than 0.4, the flow field velocity generated by the cup-shaped structure is low, resulting in the radial flow circulation failing to effectively cover the upper space of the reactor, and the mixing efficiency decreases. The same phenomenon is observed in the lower flow field when L_x/R is less than 0.4.

In the overall flow field, a significant velocity difference between the upper and lower paddles can be observed when the L_s/L_x ratio is either greater than or less than 1. When L_s/L_x is greater than 1, the flow velocity in the lower flow field is slow; when L_s/L_x is less than 1, the flow velocity in the upper flow field is slow. This results in a distinct boundary between the high-velocity and low-velocity regions of the flow field. Substances mix rapidly in the high-velocity zone, while mixing is slow in the low-velocity zone. This prevents the effective formation of fluid circulation between the upper and lower flow fields, significantly reducing the overall mixing efficiency of the flow field. When the L_s/L_x ratio equals 1, the discharge directions of the upper and lower impellers are aligned, and the flow field is vertically connected near the inner wall of the reactor without a distinct stratification boundary. This facilitates material mixing, reduces the macroscopic mixing time, and improves mixing efficiency.

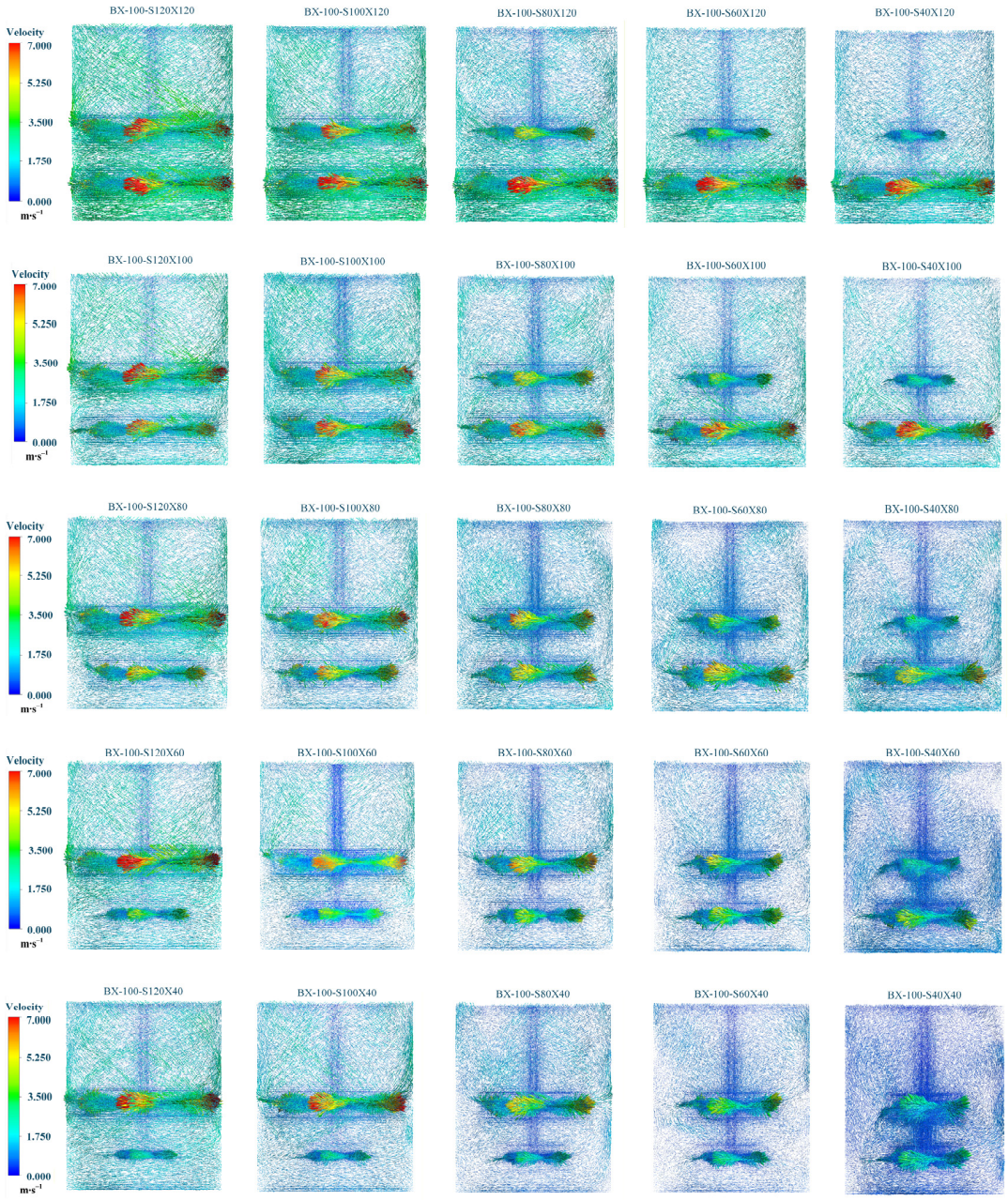


Figure 12. Velocity vector diagrams for paddles with different L_s/R and L_x/R ratios.

4. Conclusions

In this study, stirring paddle models were developed by varying the design parameters of a cup-shaped impeller (S/H, C/L_x, L_s/R, L_x/R, and L_s/L_x). Based on CFD theory, the power characteristics of these models at different rotational speeds and the flow field characteristics within the reactor were simulated and analyzed. The main conclusions are as follows:

As S/H increases, T and Np exhibit a slight upward trend, and the distance between the agitator blades has no significant effect on torque. When S/H is less than 0.333, effective circulating vortices cannot form within the system; when S/H is greater than 0.333, as the impeller spacing increases, the vortices between the impellers also become less pronounced, making it difficult to form a complete circulation. Only when S/H equals 0.333 do four stable vortices form near both sides of the dual impellers, achieving optimal mixing efficiency.

When the ratio of L_s/L_x is greater than 1 and the lower paddle length remains constant, T and Np show an upward trend as this value increases. When the ratio of L_s/L_x is less than 1 and the upper paddle length remains constant, T and Np also exhibit an upward trend as this value decreases. This indicates that as paddle length increases, torque and power consumption inevitably increase, and the increase in the length of a single layer of paddles is added to the total torque; the overall torque is determined jointly by the upper and lower L_s/R and L_x/R values.

Regarding the flow field, when L_s/R and L_x/R exceed 0.67, the mixing process fails to form a stable and complete radial circulation. When L_s/R and L_x/R are less than 0.53, the high-velocity regions in the flow field decrease, resulting in poorer mixing efficiency. When L_s/R and L_x/R are equal to 0.53, complete axial circulation is formed in both the upper and lower high-velocity zones of the flow field, significantly reducing the time required to reach a homogeneous state. A comprehensive comparison reveals that a multi-stage cup-shaped agitator with $L_s/R = 0.53$, $L_x/R = 0.53$, and $S/H = 0.333$ achieves an optimal balance between flow field velocity and power consumption.

The correlation equations related to Np about Re, L_s/R, L_x/R, $S/L_{(s,x)}$, and $C/L_{(s,x)}$ values and their range of applicability are shown below:

$Np = 0.00341Re^{-0.01221}(L_s/R)^{0.55736}(L_x/R)^{-0.04256}(S/L_x)^{13.57049}(C/L_x)^{-10.85351}$, with an error within 18% (the formula applies to Re: 10,627–1,051,809, L_s/R: 0.267–0.667, L_x/R: 0.4–0.8, S/L_x: 0.83–1.25, C/L_x: 0.5–1, $R^2 = 0.99637$).

$Np = 7.70332\ Re^{-0.01135}(L_s/R)^{7.35203}(L_x/R)^{0.57915}(S/L_s)^{11.78473}(C/L_s)^{-1.61086}$, with an error within 18% (the formula applies to Re: 10,627–1,051,809, L_s/R: 0.4–0.8, L_x/R: 0.267–0.667, S/L_s: 0.83–1.67, C/L_s: 0.5–1, $R^2 = 0.98868$).

This study focuses exclusively on two-stage impeller mixing systems and aims to investigate the effects of impeller parameters on flow field characteristics and energy consumption, based on which relevant equations have been derived. However, further research is urgently needed regarding the energy consumption, flow field characteristics, and industrial applications of three-stage and multi-stage cup-shaped impellers; this will be the focus of our next study.

Author Contributions: Conceptualization, J.B. and Q.L.; methodology, Q.L.; software, J.B.; validation, B.Z., Z.W. and Y.L. (Yang Liu); formal analysis, W.L.; investigation, L.W.; resources, H.R.; data curation, J.B.; writing—original draft preparation, J.B.; writing—review and editing, B.Z. and Z.W.; supervision, J.S.; project administration, Y.L. (Yunfei Li) and W.S. All authors have read and agreed to the published version of the manuscript.

Funding: This work is supported by the Key R&D Program of Shandong Province, (2023CXGC010601) and the Natural Science Foundation of Shandong Province (ZR2023ZD22).

Data Availability Statement: The author used SolidWorks 2022 software to design the overall geometric model and generate the graphical data. All simulation data was calculated using ANSYS Workbench 2024R1 software. Please contact the author if you require this data.

Acknowledgments: During the preparation of this manuscript, the author used DeepL (https://www.deepl.com/en, accessed on 27 July 2026) for translation. The authors have reviewed and edited the output and take full responsibility for the content of this publication.

Conflicts of Interest: Authors Yunfei Li, Wenhui Shen, and Lu Wang were employed by the company Befar Group Co., Ltd. The remaining authors declare that the research was conducted in the absence of any commercial or financial relationships that could be construed as a potential conflict of interest.

References

1. de Carvalho, R.M.; Oliveira, A.L.; Petit, H.A.; Tavares, L.M. Comparing modeling approaches in simulating a continuous pilot-scale wet vertical stirred mill using PBM-DEM-CFD. *Adv. Powder Technol.* **2023**, *34*, 104135. [CrossRef]
2. Petříček, R.; Moucha, T.; Rejl, F.J.; Valenz, L.; Haidl, J.; Čmelíková, T. Volumetric mass transfer coefficient, power input and gas hold-up in viscous liquid in mechanically agitated fermenters. Measurements and scale-up. *Int. J. Heat Mass Transf.* **2018**, *124*, 1117–1135. [CrossRef]
3. Zhang, G.; Shi, X.; Wang, F. Enhanced hydrate formation under mild conditions using a novel spiral-agitated reactor. *AIChE J.* **2022**, *68*, e17617. [CrossRef]
4. Amiraftabi, M.; Khiadani, M.; Mohammed, H.A.; Arshad, A. CFD-PBM and experimental investigation of a shear thinning fluid in a gas-liquid tank agitated by a helical ribbon impeller. *Sep. Purif. Technol.* **2021**, *272*, 118855. [CrossRef]
5. Chang, Q.; Di, S.; Xu, J.; Ge, W. Direct numerical simulation of turbulent liquid–solid flow in a small-scale stirred tank. *Chem. Eng. J.* **2021**, *420*, 127562. [CrossRef]
6. Woziwodzki, S. Mixing of viscous Newtonian fluids in a vessel equipped with steady and unsteady rotating dual-turbine impellers. *Chem. Eng. Res. Des.* **2014**, *92*, 435–446. [CrossRef]
7. Wang, X.; Farhat, M.; Fradette, L.; Tanguy, P.A. Analysis of Power Consumption in Multishaft Mixers. *Ind. Eng. Chem. Res.* **2014**, *53*, 6730–6737. [CrossRef]
8. Chapple, D.; Kresta, S.M.; Wall, A.; Afacan, A. The Effect of Impeller and Tank Geometry on Power Number for a Pitched Paddle Turbine. *Chem. Eng. Res. Des.* **2002**, *80*, 364–372. [CrossRef]
9. Jadidi, B.; Ebrahimi, M.; Ein-Mozaffari, F.; Lohi, A. Investigation of impacts of particle shape on mixing in a twin paddle blender using GPU-based DEM and experiments. *Powder Technol.* **2023**, *417*, 118259. [CrossRef]
10. Jadidi, B.; Ebrahimi, M.; Ein-Mozaffari, F.; Lohi, A. Mixing performance analysis of non-cohesive particles in a double paddle blender using DEM and experiments. *Powder Technol.* **2022**, *397*, 117122. [CrossRef]
11. Xu, H.; Guo, J.; Xu, S.; Wang, K. The Influence and Optimization of Mixing Characteristics of Feed Based on Response Surface Methodology of Stirring Paddle Structure. *Processes* **2025**, *13*, 3101. [CrossRef]
12. Armenante, P.M.; Mazzarotta, B.; Chang, G.-M. Power Consumption in Stirred Tanks Provided with Multiple Pitched-Paddle Turbines. *Ind. Eng. Chem. Res.* **1999**, *38*, 2809–2816. [CrossRef]
13. Deglon, D.; Meyer, C. CFD modelling of stirred tanks: Numerical considerations. *Miner. Eng.* **2006**, *19*, 1059–1068. [CrossRef]
14. Jaworski, Z.; Zakrzewska, B. Modelling of the Turbulent Wall Jet Generated by a Pitched Paddle Turbine Impeller. *Chem. Eng. Res. Des.* **2002**, *80*, 846–854. [CrossRef]
15. Pakzad, L.; Ein-Mozaffari, F.; Upreti, S.R.; Lohi, A. A novel and energy-efficient coaxial mixer for agitation of non-Newtonian fluids possessing yield stress. *Chem. Eng. Sci.* **2013**, *101*, 642–654. [CrossRef]
16. Ameur, H. Energy efficiency of different impellers in stirred tank reactors. *Energy* **2015**, *93*, 1980–1988. [CrossRef]
17. Guo, C.; Xue, S.; Li, W.; Qin, H.; Guo, J.; Zhang, J. Investigation of power characteristics in a novel cup-shaped-paddle mixer. *Chem. Eng. Process. Process Intensif.* **2018**, *125*, 150–162. [CrossRef]
18. Zhao, S.; Guo, J.; Dang, X.; Ai, B.; Zhang, M.; Li, W.; Zhang, J. Energy consumption, flow characteristics and energy-efficient design of cup-shape paddle stirred tank reactors: Computational fluid dynamics and artificial neural network investigation. *Energy* **2022**, *240*, 122474. [CrossRef]
19. Dang, X.; Guo, J.; Yang, L.; Xue, S.; Ai, B.; Li, X.; Chen, L.; Li, W.; Qin, H.; Zhang, J. Effects of paddle structures on the dissolution and gas-liquid mass transfer performance of cup-shaped paddle mixers. *J. Taiwan Inst. Chem. Eng.* **2022**, *131*, 104195. [CrossRef]
20. Zhang, P.; Li, W.; Liu, Y.; Chi, R.; Long, B.; Zhang, J. Investigation on drawdown process of light-floating particles in a pilot scale cup-shaped paddle agitator. *Chem. Eng. Process. Process Intensif.* **2024**, *201*, 109819. [CrossRef]
21. Bouaifi, M.; Roustan, M. Power consumption, mixing time and homogenisation energy in dual-impeller agitated gas–liquid reactors. *Chem. Eng. Process. Process Intensif.* **2001**, *40*, 87–95. [CrossRef]
22. Kondo, S.-I.; Yamada, N.; Takahashi, K. Distribution of Solid Particles Lighter than Liquid in an Agitated Vessel Stirred by Dual Impellers. *J. Chem. Eng. Jpn.* **2008**, *41*, 155–160. [CrossRef]
23. Gu, D.; Liu, Z.; Tao, C.; Li, J.; Wang, Y. Design of Impeller Paddles for Intensification of Gas-Liquid Dispersion Process in a Stirred Tank. *Int. J. Chem. React. Eng.* **2018**, *16*, 20180022. [CrossRef]
24. Russell, A.W.; Piccione, P.M.; Luckham, P.F.; Pervunin, K.S.; Markides, C.N. An experimental study of the mixing characteristics of viscoplastic fluids in dual-impeller agitation systems. *Chem. Eng. Res. Des.* **2025**, *216*, 216–229. [CrossRef]
25. Gu, Q.; Yu, J.; Liu, Y.; Wang, Y.; Zhuang, Y.; Li, C. Multiscale CFD-metabolic modeling reveals hybrid impeller configurations mitigate substrate and oxygen starvation in industrial bioreactors. *Biochem. Eng. J.* **2026**, *226*, 109956. [CrossRef]
26. Věříšová, M.; Dostál, M.; Jirout, T.; Petera, K. Heat transfer in a jacketed agitated vessel equipped with multistage impellers. *Chem. Pap.* **2015**, *69*, 690–697. [CrossRef]

27. Heyter, A.; Wollny, S. Influence of Different Baffle Variations on the Effectiveness of Multi-Stage Agitated Vessels. *Chem. Ing. Tech.* **2017**, *89*, 416–423.
28. Qin, S.; Zhang, J.; Zhang, J.; Zhao, D.; Xu, X.; Jiang, D. Study on Mixing Performance of High-Viscosity Fluid in Continuous Microfluidic Multistage Stirrer. *Ind. Eng. Chem. Res.* **2025**, *64*, 6407–6419. [CrossRef]
29. Yakhot, V.; Smith, L.M. The renormalization group, the ε-expansion and derivation of turbulence models. *J. Sci. Comput.* **1992**, *7*, 35–61. [CrossRef]
30. Yakhot, V.; Orszag, S.A. Renormalization group analysis of turbulence. I. Basic theory. *J. Sci. Comput.* **1986**, *1*, 3–51. [CrossRef]
31. Lai, Y.G. Predictive Capabilities of Turbulence Models for a Confined Swirling Flow. In Proceedings of the ASME 1994 International Mechanical Engineering Congress and Exposition, Chicago, IL, USA, 6–11 November 1994; pp. 93–104. [CrossRef]
32. Gopalakrishnan, B.; Saravana Kumar, G.; Prakash, K.A. Parametric analysis and optimization of gas-particle flow through axial cyclone separator: A numerical study. *Adv. Powder Technol.* **2023**, *34*, 103959. [CrossRef]
33. Yingna, L. Numerical Simulation of the Three-dimensional Flow Field in Stirred Tank with Double Straight and Inclined Impeller and Its Combination. *Chin. J. Mech. Eng.* **2008**, *44*, 290–297. [CrossRef]
34. Liu, Q.; Qin, Y.; Zhu, G.; Zhang, X.; Wang, F.; Li, G.; Liu, S.; Zhang, Z.; Zhu, B.; Wang, Z. Numerical simulation of power and flow field characteristics of different spiral stirred reactors. *Chin. J. Chem. Eng.* **2025**, *78*, 218–231. [CrossRef]
35. Papkov, V.; Shadymov, N.; Pashchenko, D. Gas flow through a packed bed with low tube-to-particle diameter ratio: Effect of pellet roughness. *Phys. Fluids* **2024**, *36*, 027127. [CrossRef]
36. Pashchenko, D. Flow dynamic in a packed bed filled with Ni-Al_2O_3 porous catalyst: Experimental and numerical approach. *AIChE J.* **2019**, *65*, e16558. [CrossRef]
37. Hoseini, S.S.; Najafi, G.; Ghobadian, B.; Akbarzadeh, A.H. Impeller shape-optimization of stirred-tank reactor: CFD and fluid structure interaction analyses. *Chem. Eng. J.* **2021**, *413*, 127497. [CrossRef]
38. Liu, Q.; Zhang, X.; Xiong, X.; Wang, F.; Li, G.; Liu, S.; Shen, Q.; Zhang, Z.; Qin, Y.; Zhu, B.; et al. CFD simulation of power characteristics and flow field distribution of different spiral stirring paddles. *Chem. Eng. Process. Process Intensif.* **2024**, *205*, 110033. [CrossRef]
39. Gillissen, J.J.J.; Van den Akker, H.E.A. Direct numerical simulation of the turbulent flow in a baffled tank driven by a Rushton turbine. *AIChE J.* **2012**, *58*, 3878–3890. [CrossRef]

Disclaimer/Publisher's Note: The statements, opinions and data contained in all publications are solely those of the individual author(s) and contributor(s) and not of MDPI and/or the editor(s). MDPI and/or the editor(s) disclaim responsibility for any injury to people or property resulting from any ideas, methods, instructions or products referred to in the content.